ACCSCIENCE PUBLISHING

International Journal of Bioprinting

RESEARCH ARTICLE

Evaluation of biomechanical properties and early osseointegration of biomimetic bone trabecular Ti6Al4V scaffolds based on Voronoi design

Jinghong Yang[1,2†], Zi Wang[1,3,4†], Lujun Jiang[1,3,4†], Zhong Li[1,3,4*], Linlin Liu[5*], and Juncai Liu[1,3,4*]

[1]Department of Orthopedics, The Affiliated Hospital, Southwest Medical University, Luzhou, Sichuan, China

[2]Department of Orthopaedic Surgery, The First Affiliated Hospital of Chongqing Medical University, Chongqing, China

[3]Stem Cell Immunity and Regeneration Key Laboratory of Luzhou, Southwest Medical University, Luzhou, Sichuan, China

[4]Sichuan Provincial Laboratory of Orthopaedic Engineering, Southwest Medical University, Luzhou, Sichuan, China

[5]School of Integrated Circuits, Chongqing University of Posts and Telecommunications, Chongqing, China

[†]These authors contributed equally to this work.

***Corresponding authors:**
Zhong Li
(lizhong403@swmu.edu.cn)

Linlin Liu
(1102584187@qq.com)

Juncai Liu
(liujuncai011218@163.com)

Citation: Yang J, Wang Z, Jiang L, Li Z, Liu L, Liu J. Evaluation of biomechanical properties and early osseointegration of biomimetic bone trabecular Ti6Al4V scaffolds based on Voronoi design. *Int J Bioprint*. 2025;11(6):311-326. doi: 10.36922/IJB025310311

Received: July 31, 2025
Revised: September 18, 2025
Accepted: September 22, 2025
Published online: September 22, 2025

Abstract

Ti6Al4V scaffolds demonstrate significant translational potential for bone defect reconstruction by virtue of their exceptional biocompatibility and corrosion resistance. However, achieving concurrent osseointegration enhancement and mechanical compatibility with native cancellous bone remains a critical design constraint. A trabecular bone-mimetic porous Ti6Al4V scaffold was fabricated via Voronoi-tessellated computer-aided design and selective laser melting. Precise modulation of pore architecture enabled controlled porosity. The mechanical properties of the scaffold were characterized through compression testing. Early-stage *in vivo* osseointegration was evaluated at weeks 4 and 12 in a rabbit femoral condyle defect model using histomorphometry and micro-computed tomography, with comparisons made against conventional strut-based and G-curved lattice structures. The Voronoi scaffold demonstrated an elastic modulus and yield strength comparable to cancellous bone, thereby mitigating stress-shielding effects. Additionally, according to the results from the biomechanics, computational fluid dynamics, and *in vivo* analyses, the scaffold demonstrated significantly enhanced osteogenic potential and superior bone-implant interface integration compared to the strut and triply periodic minimal surface (TPMS) designs. In conclusion, the Voronoi design provides an effective biomimetic strategy for fabricating porous titanium alloy bone scaffolds with enhanced osteogenic properties, which embody higher potential than conventional struts and TPMS structures in facilitating bone defect repair.

Keywords: Biomechanics; Computational fluid dynamics; Osseointegration; Ti6Al4V scaffolds; Voronoi

1. Introduction

Titanium and its alloys have been widely used in clinical applications for over four decades due to their exceptional biocompatibility and corrosion resistance.[1] In recent years, titanium alloy bone scaffolds have gained significant attention as a promising solution for repairing bone defects that exceed the critical defect threshold. These scaffolds are increasingly recognized as a viable option in orthopedic applications. Titanium alloys exhibit a relatively low Young's modulus (7–30 GPa) compared to other metallic materials, which, although higher than natural bone, results in a significantly reduced stress shielding effect compared to materials such as tantalum and stainless steel. This makes titanium alloys more favorable for bone repair applications. Additionally, titanium implants demonstrate superior compatibility with host bone tissue, reducing bone resorption and implant loosening.[2]

Recent advancements in 3D printing technologies, including selective laser melting (SLM), selective laser sintering, and electron beam melting, have enabled the precise fabrication of porous titanium alloy scaffolds with controllable microstructures.[3–7] By leveraging computer-aided design (CAD) methodologies, researchers can create intricate porous architectures with precisely controlled porosity and interconnectivity.[8] These techniques offer several advantages, such as streamlined construction processes, enhanced feasibility for mechanical evaluations, and rapid prototyping. Consequently, there has been a surge in research efforts by scientists and orthopedic surgeons to develop 3D-printed porous bone scaffolds.

Contemporary advancements in bone tissue engineering have focused on developing porous titanium alloy scaffolds that mimic the hierarchical architecture and multifunctional performance of natural bone. These biomimetic constructs aim to balance often-conflicting requirements, including mechanical load-bearing capacity, osteoconductive porosity, and dynamic biological responsiveness. Critical studies by Gryko et al.[9] using finite element analysis identified 40% porosity as the optimal threshold for maximizing osseointegration rates, highlighting pore architecture as a key factor in bone-scaffold interfacial remodeling. Complementary work by Arjunan et al.[7] systematically quantified how pore morphology in Ti6Al4V scaffolds governs mechanical performance, demonstrating nonlinear correlations between strut geometry and permeability, stiffness, and stress concentration factors.

Emerging Voronoi tessellation-derived scaffolds represent a paradigm shift toward stochastic biomimicry. These structures replicate the anisotropic, non-periodic topology of natural bone trabeculae through Dirichlet spatial segmentation, achieving biomechanical compatibility, enhanced biofluid dynamics, and angiogenic potential.[10] However, while the stochastic nature of Voronoi structures—resulting from the spatial distribution of seed points that generate variations in cell size, shape, and connectivity—mimics the non-periodic architecture of natural trabecular bone, it also introduces unpredictability in stress distribution, leading to localized stress concentrations as high as 2.8× ambient levels, compared to 1.9× in the curved scaffold. This necessitates advanced topology optimization algorithms to mitigate fracture risks at sharp edges. Recent innovations in SLM have enabled the fabrication of Voronoi scaffolds, which maximize osteogenic differentiation while maintaining non-cytotoxicity, as demonstrated by Chen et al.[11]

In contrast, triply periodic minimal surface (TPMS) structures, based on mathematical implicit function generation, leverage mathematical periodicity to achieve mechanical reliability, stress homogenization, and manufacturing precision.[12–15] While TPMS scaffolds demonstrate superior bone-implant contact, their uniform porosity distribution limits vascular infiltration. This dichotomy in biological performance underscores the need for anatomically stratified design strategies: Voronoi's stochastic networks may benefit vascularized defects, whereas the mechanical predictability of TPMS structures makes them well-suited for load-critical applications.[16] Additionally, conventional strut-based scaffolds offer predictable mechanical properties but may be compromised by stress shielding, biofluidic stagnation, and inadequate osteogenic stimulation, which limit the scaffolds' overall performance.[17,18]

In this study, we optimized porous bone scaffolds by evaluating three distinct structures—conventional strut-based, G-curved (TPMS), and Voronoi-trabecular biomimetic architectures—through computational modeling, mechanical testing, and animal experiments. The mechanical properties and early-stage osteogenesis of scaffolds with identical pore sizes (500 μm) and porosities (60%) were systematically assessed. The pore size of 500 μm and porosity of 60% were chosen based on previous studies indicating that this range optimally supports bone ingrowth and vascularization while maintaining mechanical strength.[11]

Mechanical characterization confirmed that all scaffolds met *in vivo* load-bearing requirements. *In vivo* evaluation involved the use of micro-computed tomography (micro-CT) reconstruction and histomorphometric analysis at weeks 4 and 12 in rabbit distal femurs bilaterally implanted with the scaffolds. These

analyses revealed architecture-dependent osteogenesis patterns. Complementary computational fluid dynamics (CFD) simulations quantitatively correlated pore topology with hydrodynamic parameters, elucidating the mechanobiological mechanisms underlying the observed differences in bone ingrowth.

2. Materials and methods

2.1. Design and manufacturing of scaffolds

Three distinct lattice architectures were investigated in this study: (i) a body-centered cubic strut-based configuration (strut), (ii) a TPMS geometry following G-surface topology (curved), and (iii) a biomimetic trabecular bone structure based on the Voronoi algorithm (Voronoi). The modeling workflow was implemented using Unigraphics NX (Siemens PLM Software, Germany) with differential approaches for each architecture.

The body-centered cubic configuration was reproduced following our previously validated modeling methodology,[19] as illustrated in Figure 1A. For the TPMS architecture, the G-surface geometry was mathematically defined using the implicit surface equation (**Equation I**), generating the curvature-dominated structure shown in Figure 1B. The Voronoi structure employed a stochastic generation process: ten seed points were randomly distributed within a $2 \times 2 \times 2$ mm^3 volumetric space, followed by application of the Voronoi tessellation algorithm. Polyhedral edges from the tessellated domains were converted into cylindrical pillars to create the bioinspired porous network depicted in Figure 1C.

$$G: \sin(\omega x)\cos(\omega y) + \sin(\omega y) \cos(\omega z) + \sin(\omega z)\cos(\omega x) = 0 \quad (I)$$

where $\omega = 2\pi/L$, and L is the length of the structural unit.

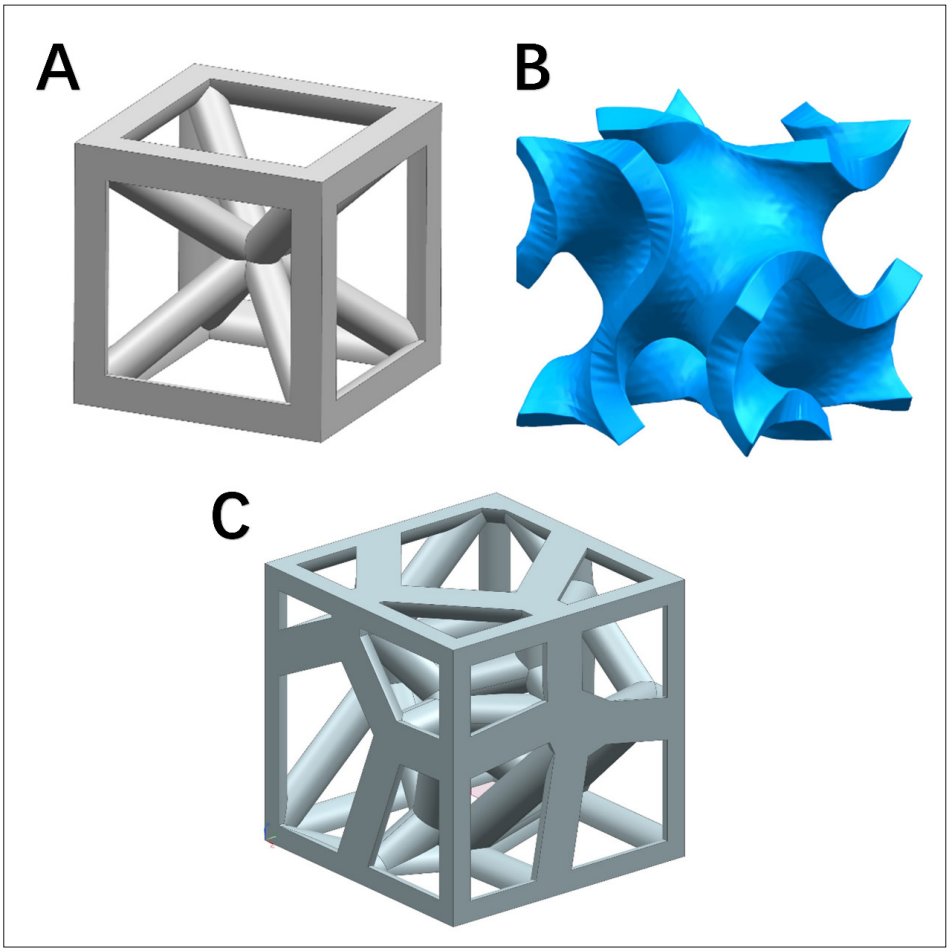

Figure 1. Schematic designs of the three structures: (A) Strut; (B) G Curve; (C) Voronoi.

All scaffolds were fabricated using SLM with the following parameters: laser power of 500 W, spot size of 50 μm, and layer thickness of 20 μm.

2.2. Characterization of the scaffolds

Three-dimensional structural characterization of the porous titanium scaffold, fabricated via SLM, was performed through micro-CT imaging (Figure 2). Following tomographic acquisition, Mimics 21.0 (Materialise, Italy), a medical image processing platform, was used to facilitate comprehensive three-dimensional reconstruction and quantitative morphometric analysis of scaffold architecture and peri-implant osseous tissue.

2.3. Mechanical properties of the scaffolds

Mechanical testing was conducted in accordance with ISO-13314, the international standard for compressive testing of porous and cellular metals. Rectangular scaffolds (n = 5; dimensions: 10 × 10 × 12 mm) were subjected to compressive strength tests using a universal testing machine (E10000 Model; Instron Company, United States) at a compression rate of 1 mm/min (Figure 3A). The elastic modulus (E) and compressive strength (σ) were derived from the material's stress–strain curve. The elastic modulus was determined as the maximum slope in the elastic region, while the yield strength was determined using the 0.2% offset method, a standard technique for metallic materials without a distinct yield point. This method involves constructing a line parallel to the elastic portion of the stress–strain curve but offset by 0.2% strain; the stress value at the intersection of this line and the curve is defined as the yield strength.

2.4. Surgical procedure

Eighteen adult male New Zealand rabbits (2.5–3.0 kg) were obtained from the Laboratory Animal Center of Southwest Medical University for this study. The rabbits were housed

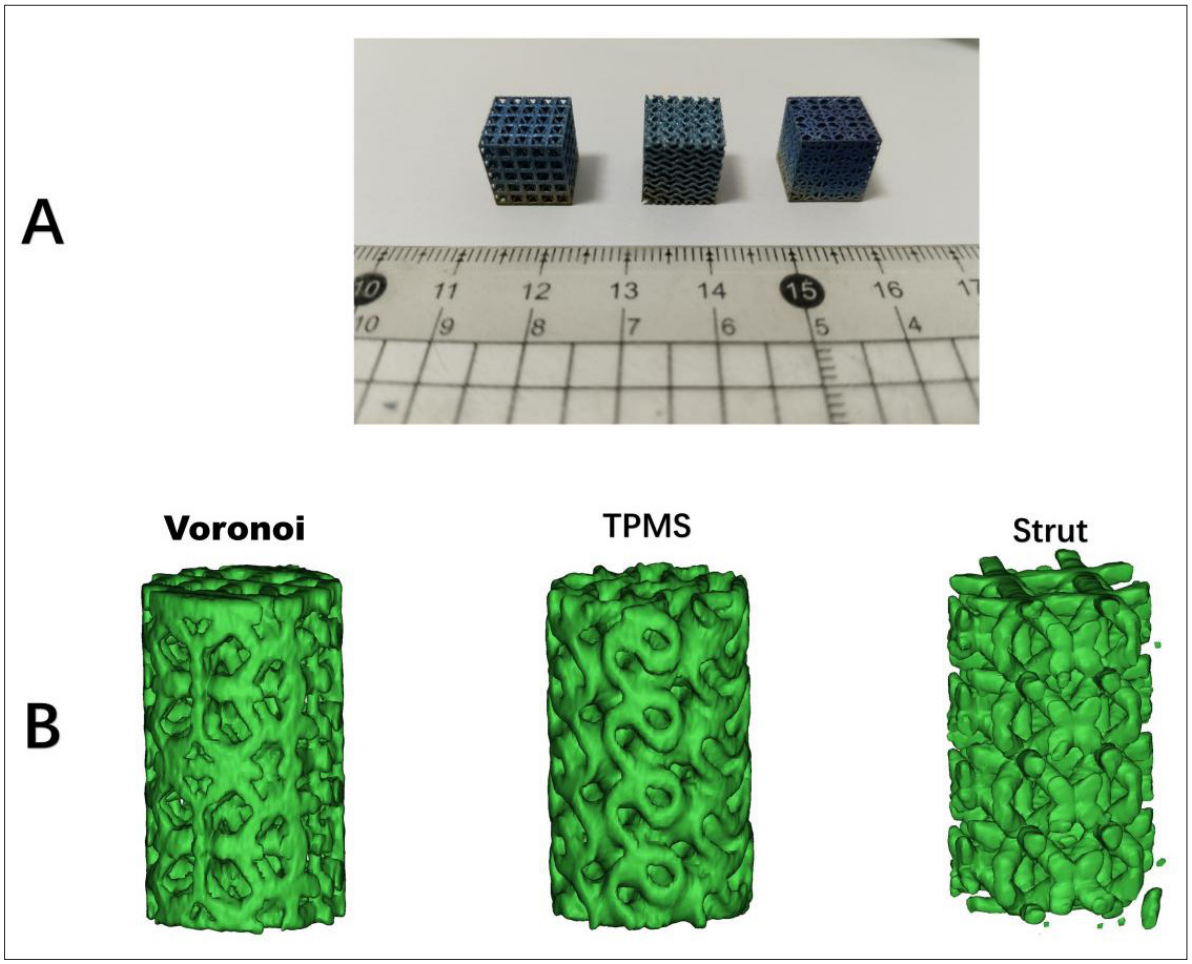

Figure 2. Photograph of the three 3D-printed titanium stents (A), and micro-CT reconstruction of the three porous titanium stents (B). Abbreviations: Micro-CT, micro-computed tomography; TPMS, triply periodic minimal surface.

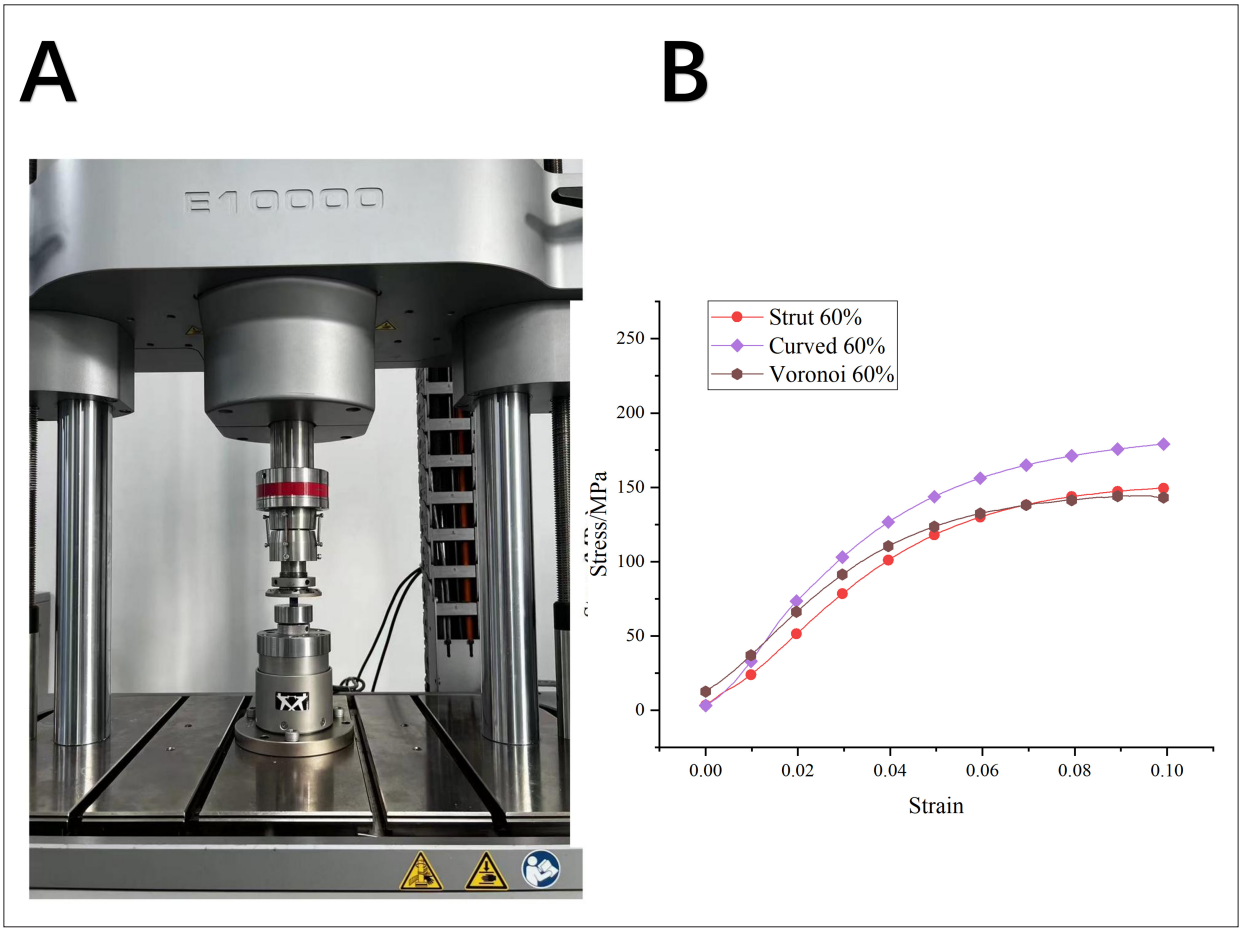

Figure 3. Universal Testing Machine (E10000 Model, Instron Company) (A), and stress–strain curves of the three scaffold specimens (B).

in a controlled environment with a temperature of 24°C and humidity of 60%, with free access to food and water. The experimental protocols involving animals were approved by the Ethics Committee of the Affiliated Hospital of Southwest Medical University to safeguard the welfare of laboratory animals, in compliance with international standards such as the Declaration of Helsinki. The rabbits were randomly assigned to three groups based on the duration of implantation (6 or 12 weeks). In each group, 18 femurs from 18 rabbits were implanted with three types of cylindrical scaffolds, each with distinct structures.

General anesthesia was induced using intravenous 3% sodium pentobarbital (30 mg/kg), supplemented with local anesthesia using 0.5% lidocaine. Following skin preparation and disinfection, a 3 cm longitudinal incision was made at the femoral condyle (Figure 4A). The skin and subcutaneous tissue were incised, the muscles were separated, and the periosteum was cut to expose the femoral condyle. A hole with a diameter of 5 mm and a depth of 8 mm was made in the lateral femoral condyle using a low-speed drill (Figure 4B). To prevent thermal necrosis, the drilling site was continuously irrigated with saline solution. After scaffold implantation (Figure 4C), the wound was closed in layers. Postoperative anti-infective treatment was administered via intramuscular injection of cephalosporin antibiotics for three days.

At 4 and 12 weeks post-implantation, euthanasia was performed via intravenous air injection, followed by harvesting of the femurs. The harvested femurs were rinsed with formalin, dehydrated in ethanol, infiltrated, embedded, and sectioned into 200 μm slices using an EXAKT E300CP hard tissue slicer (Germany). The slices were ground and polished to produce thin sections of approximately 70 μm. Hematoxylin and eosin staining was applied, and the sections were examined under a light microscope (Olympus, Japan) to evaluate the presence of new bone tissue, microvascular structures, or fibrous tissue within the scaffolds.

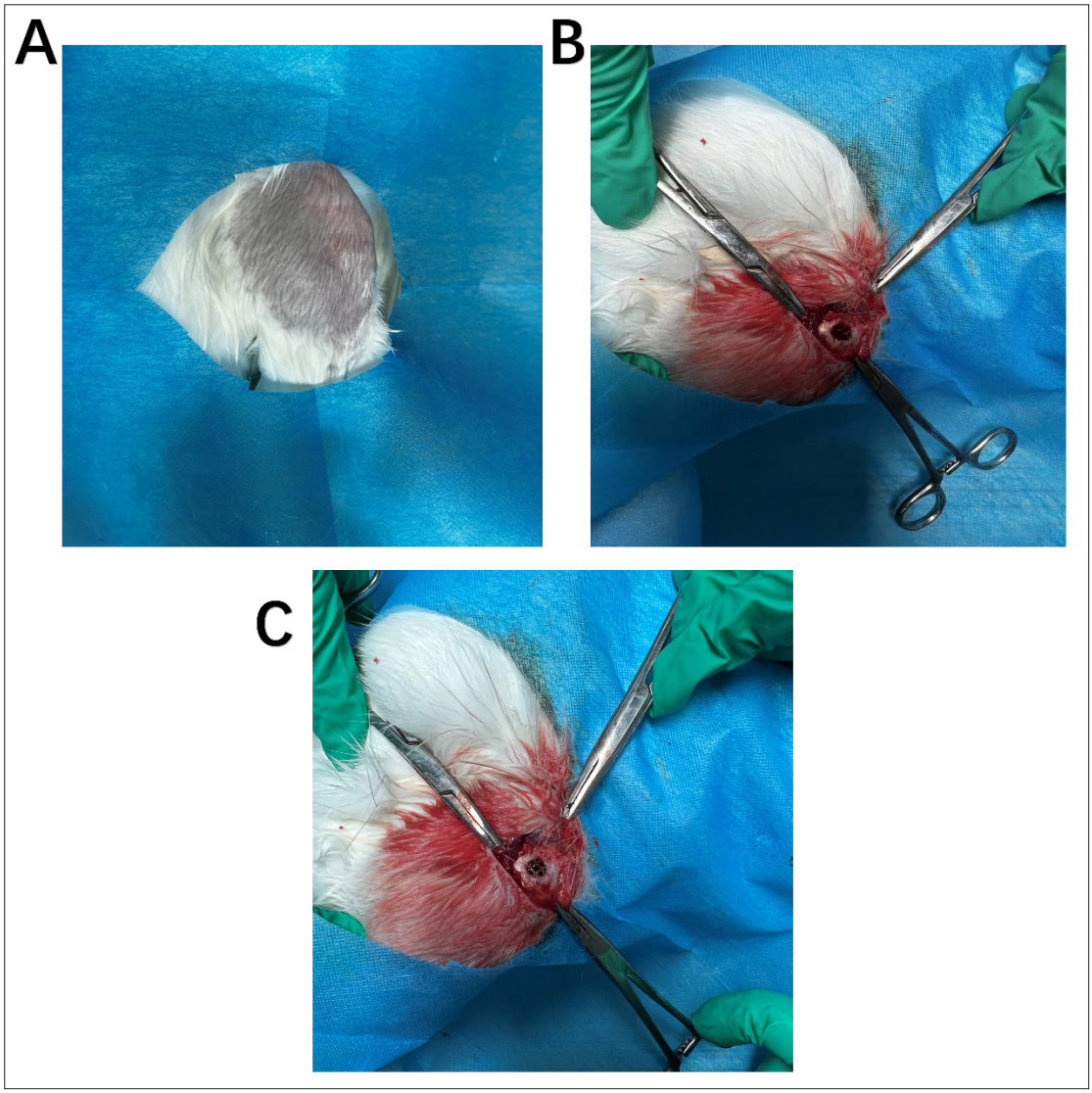

Figure 4. Surgical procedure for scaffold implantation. (A) Peeling and exposing the surgical site. (B) Creating a cylindrical defect—a hole with a diameter of 5 mm and a depth of 8 mm to match the scaffold's size—in the lateral femoral condyle of a rabbit using a low-speed drill. (C) Implanting a titanium scaffold into the femoral condylar osseous defect.

2.5. Micro-computed tomography analysis

To assess new bone formation, micro-CT (Micro-CT100, SCANCO Medical AG, Switzerland) was used to scan the rabbit femurs implanted with porous scaffolds. The scanning parameters were set as follows: X-ray source voltage of 90 kV, a beam current of 200 μA, and a resolution of 17.2 μm. After scanning, the images were reconstructed and segmented into binary forms for further analysis using Mimics 21.0 (Materialise, Belgium). The region of interest was defined as the scaffold's internal volume and the bone tissue ingrowth. Bone volume (BV) and total pore volume (TV) were measured by micro-CT, and the BV/TV ratio was calculated to quantitatively assess bone ingrowth. A higher BV/TV ratio indicates enhanced bone formation within the scaffold.

2.6. Histological evaluation

The femoral condyle was first fixed, then dehydrated with ethanol, and embedded in methyl methacrylate. A 50 μm-thick slice was cut along the longitudinal axis of the cylindrical scaffold using a saw blade. The section was subsequently stained with 1.2% trinitrophenol and 1% acid magenta (Van-Gieson staining). Finally, the stained sample was examined using a fluorescence microscope (Olympus, Japan) for analysis.

2.7. Computational fluid dynamics simulation

CFD was employed to assess permeability, flow velocity, and internal velocity streamlines of various scaffolds. To reduce computational time, the analysis was limited to 2 × 2 unit cells, taking advantage of the structural symmetry. The Navier–Stokes equations[20] were applied under the assumption that the fluid behaves as an incompressible medium.

$$\rho\frac{\theta v}{\theta t} - \mu\nabla^2 V + \rho\left(v \bullet \nabla\right)v + \nabla p = F,\ \nabla.V = 0 \qquad \text{(II)}$$

where ρ, v, and μ represent the density (kg/m³), flow velocity (m/s), and dynamic viscosity (kg/m/s) of the fluid, respectively; ∇ stands for the del operator; p refers to pressure (MPa); and F represents force (N). The permeability κ of the three scaffold designs was computed based on Darcy's law:

$$\kappa = \frac{v.\mu.L}{\Delta P} \qquad \text{(III)}$$

where v denotes the fluid inlet velocity (measured in m/s), L represents the characteristic length of the model (in meters), and ΔP corresponds to the pressure differential across the system (expressed in MPa).

The CFD simulation model was subjected to analysis and computation utilizing Ansys Fluent software (Ansys, United States). During the computational process, specific boundary conditions were assigned: the inlet velocity was established at a value of 0.1 mm/s, the outlet pressure was configured to 0, the fluid density was designated as 1050 kg/m³, and the viscosity was set to 0.0037 kg/(m·s).[21] Additionally, a supplementary fluid domain positioned above the structural configuration was incorporated to mitigate potential boundary effects.

2.8. Finite element analysis

Static structural analysis was carried out on the three scaffold models using the Ansys Static Structural module. The material was modeled as an isotropic linear elastic titanium alloy (Ti6Al4V), with an elastic modulus of 110 GPa and a Poisson's ratio of 0.3. Boundary conditions simulated a porous structural environment: the base was fixed, the side walls were left free, and a compressive force of 10 N was applied normally to the top surface. The resulting stress distributions were analyzed to evaluate pressure variations throughout the scaffold.

2.9. Statistical analysis

The statistical analysis was conducted using the SPSS software (SPSS Inc., Chicago, IL, United States). All data are expressed as the mean ± standard deviation. One-way analysis of variance was employed for data analysis. In every instance, statistical significance was defined as $p < 0.05$.

3. Results

3.1. Mechanical properties of the scaffold

Figure 3B presents the stress–strain curves of three strut specimens, revealing yield strengths comparable to the TPMS structure. Experimental elastic moduli and yield strengths are shown in Table 1. While trabecular bone exhibits an elastic modulus of 0.1–4.5 GPa and yield strengths of 0.56–55.3 MPa in the proximal tibia/femur, all investigated structures demonstrate significantly higher mechanical properties. Their elastic moduli (1.9–4.2 GPa) correspond well with host bone tissue requirements. Consequently, these scaffolds achieve bone-matching stiffness and enhanced yield strength, demonstrating significant potential for bone tissue engineering applications.

3.2. Micro-computed tomography analysis

Titanium scaffolds were implanted in rabbit distal femurs and explanted at weeks 4 and 12 for micro-CT analysis of bone formation. Three-dimensional reconstructions (Figure 5A) demonstrate progressive bone ingrowth within scaffolds over time. Quantitative analysis revealed distinct osseointegration patterns across scaffold types, consistent with the BV/TV ratios (Figure 5B). BV/TV measurements for strut, curved, and Voronoi structures at weeks 4 and 12 are 6.7%/9.3%, 9.1%/11%, and 9.1%/16%, respectively.

3.3. Histological analysis

Animals were sacrificed at 4 and 12 weeks. Harvested samples were fixed in 5% polyformaldehyde, dehydrated through a graded ethanol series (70%–100%), and embedded with poly(methylmethacrylate) (Cool-Set-A, Aorigin, China). Sections (10–20 μm) were prepared using a diamond histological saw (SAT-001, Origin, China) and stained with methylene blue/basic fuchsin (Sigma). Qualitative assessment of bone growth was performed on stained sections (Figure 6), revealing progressive bone

Table 1. Elastic modulus and yield strength of the three types of scaffolds tested

Scaffold type	Elastic modulus, E (GPa)	Yield strength, σ (MPa)
Strut	2.5	120
Curved	2.6	144
Voronoi	2.25	135

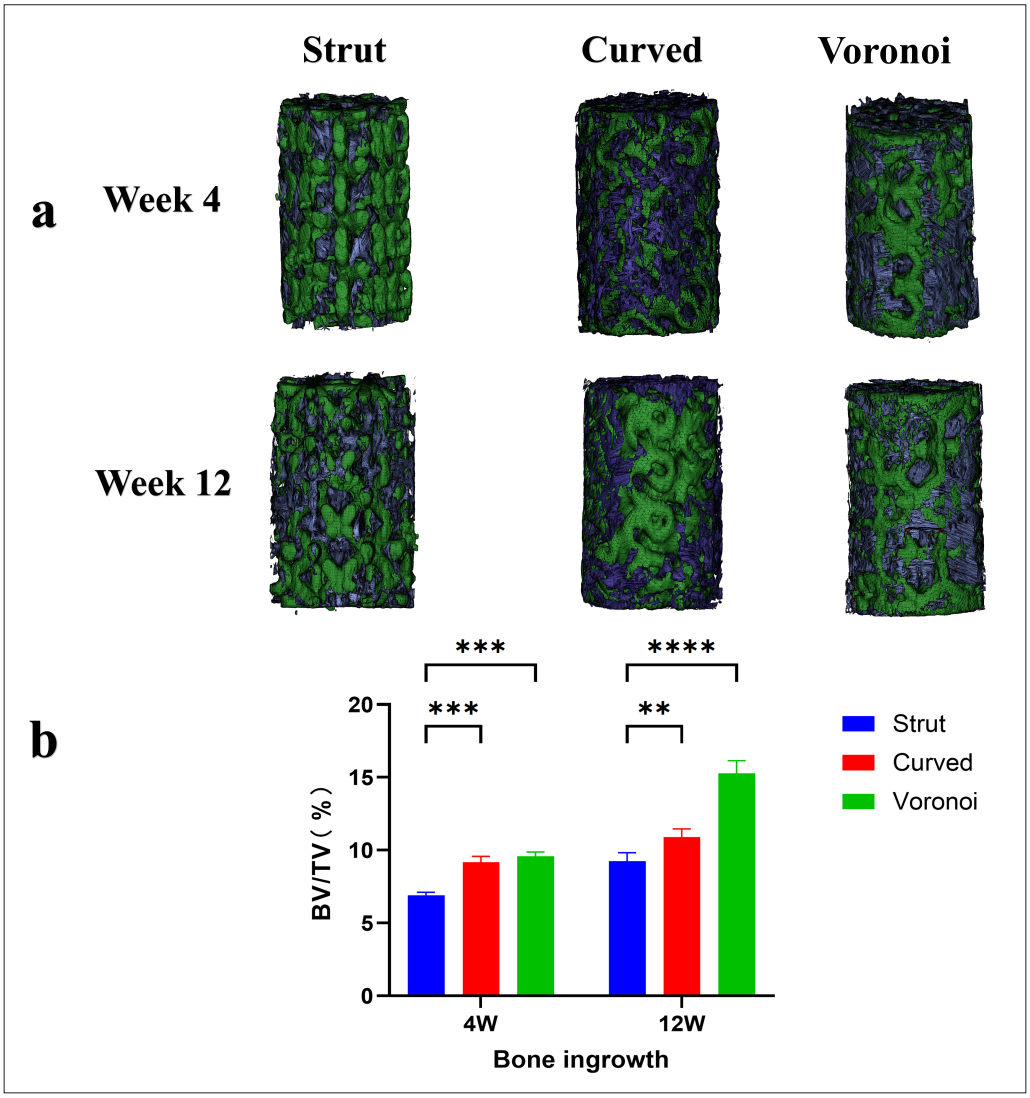

Figure 5. Micro CT image and results. (A) Micro-CT reconstruction of the distal femur of a rabbit at 4 and 12 weeks post-implantation of titanium scaffold. Green color represents the bone scaffold, and blue color represents newly formed bone. (B) BV/TV measurements for implanted scaffolds (**$p < 0.01$, ***$p < 0.001$; ****$p < 0.0001$).

tissue formation within scaffold pores over time. The highest volume of new bone formation was observed in the Voronoi structure, whereas the lowest volume was detected in the strut architecture. These findings align consistently with both the qualitative and quantitative micro-CT analyses. Therefore, histological sectioning results corroborated the experimental data, confirming their validity.

3.4. Computational fluid dynamics analysis

Fluid flow permeability and velocity within scaffolds significantly influence bone tissue regeneration.[22] While interstitial fluid transport delivers essential oxygen and nutrients to cells, excessive permeability impedes cellular adhesion, whereas insufficient permeability compromises nutrient supply.[23]

Figure 7A shows the pressure distribution maps of the stents. The pressure decreases gradually from the highest point at the inlet to the lowest point at the outlet. As shown in the pressure maps (Figure 7A), the pressure decreased gradually from the inlet to the outlet in all three structures. However, the spatial distribution of pressure varied significantly: the strut structure exhibited the most continuous and uniform pressure gradient along its straight channels. In contrast, the TPMS structure showed noticeable localized pressure concentrations at the regions of high curvature, while the Voronoi structure

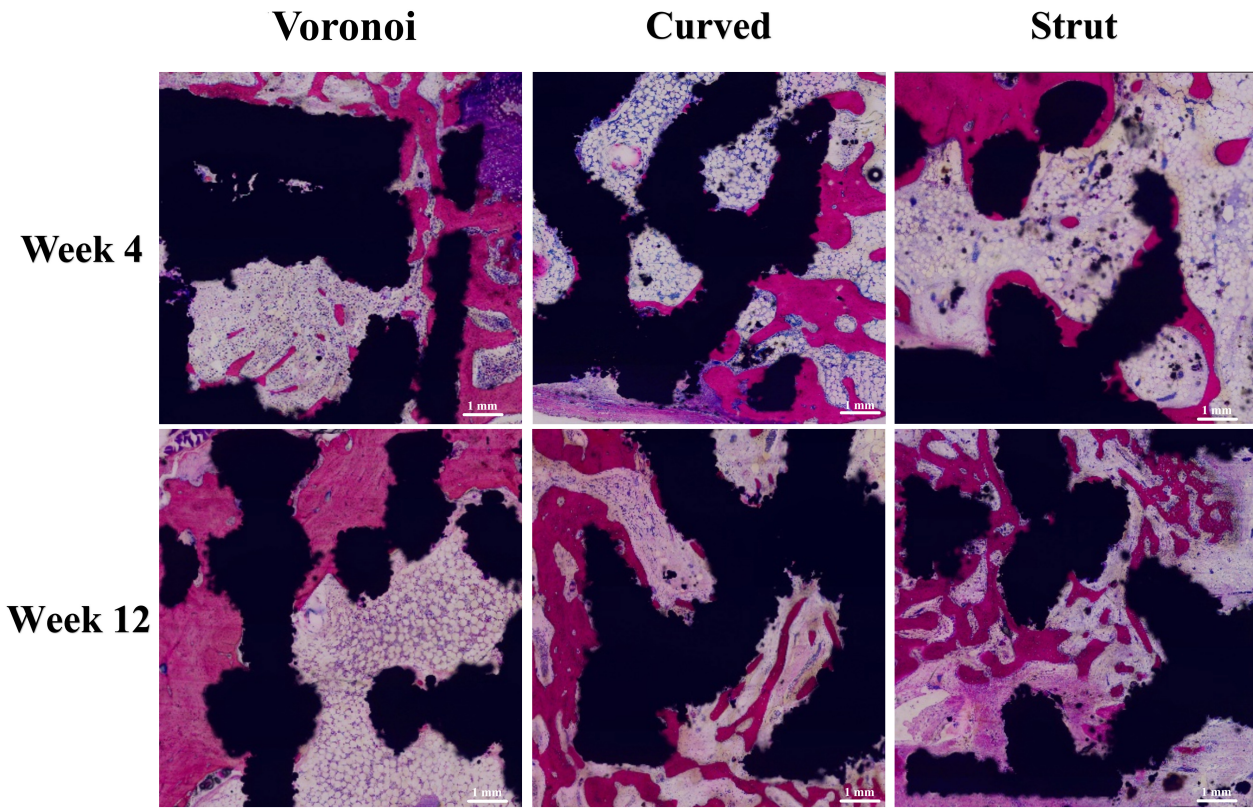

Figure 6. Stained tissue sections of bone specimens at 4 and 12 weeks post-implantation of scaffolds. Red region represents bone tissue, and black region represents scaffolds. Magnification: 10×; scale bar: 1 mm.

demonstrated a more heterogeneous but interconnected pressure distribution, with moderate variations corresponding to its irregular pore morphology.

Figure 7B presents the permeability (κ) of the three scaffold architectures, calculated using **Equation III**. The measured κ values (2.3×10^{-9} to 5.49×10^{-9} m^2) fall within the physiological range reported for proximal tibia (0.467×10^{-9} to 14.8×10^{-9} m^2).[24]

Figure 7C quantifies the pressure differential (ΔP) between the inlet and outlet across the three scaffold architectures. The strut structure shows a relatively small pressure gradient, while the curved structure shows the highest ΔP, and the Voronoi structure displayed an intermediate pressure differential. This pronounced disparity indicates that the strut structure's internal geometry significantly impedes fluid transport, reducing hydrodynamic efficiency and limiting perfusion throughout its internal domains.

Figure 8 presents flow velocity distributions within three scaffold architectures. The Voronoi structure exhibits reduced internal flow velocities relative to comparative designs, which are advantageous for cellular adhesion to scaffold surfaces, thus allowing for enhanced osteogenesis *in vivo*. Conversely, significantly elevated velocities at strut junctions versus pore regions in other structures facilitate cellular infiltration into deeper zones, thereby inhibiting surface adhesion. Consequently, the Voronoi architecture demonstrates superior cellular proliferation compared to its counterparts.

3.5. Results of finite element analysis

Based on the finite element analysis results (Figure 9), the equivalent (von Mises) stress distributions under static structural loading reveal significant mechanical differences among the three scaffold architectures. The strut structure exhibited the maximum von Mises stress of 45.572 MPa, indicating superior stress distribution and mechanical efficiency. The Voronoi structure showed an intermediate peak stress value of 71.714 MPa, reflecting its biomimetic design's ability to mitigate stress concentrations effectively. In contrast, the curved structure endured the highest stress level of 103.71 MPa, suggesting a higher risk of

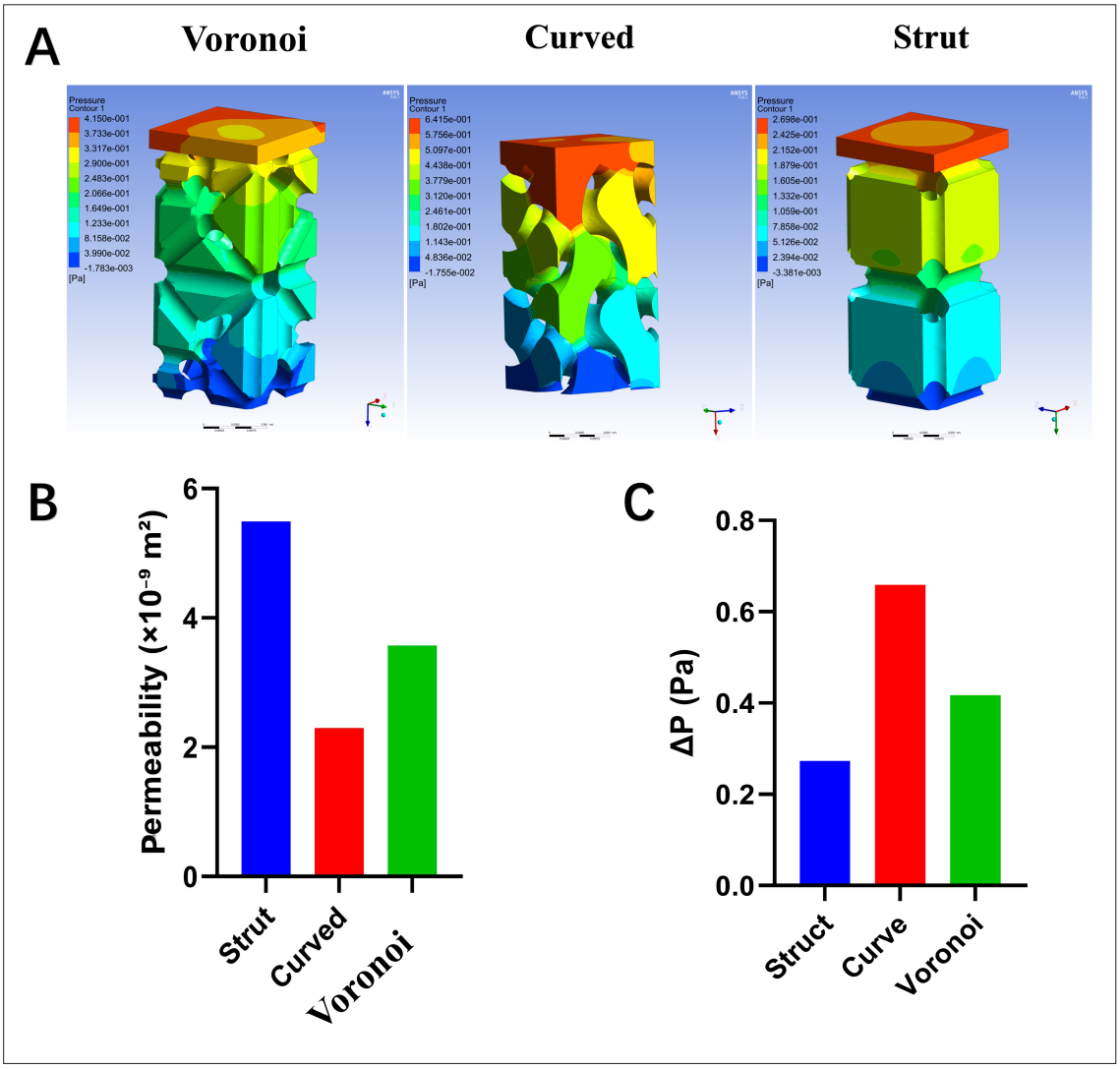

Figure 7. Fluid simulation results across the three types of scaffolds: (A) pressure distribution map; (B) permeability (κ); (C) pressure differential (ΔP).

stress shielding and potential mechanical failure under load. These results highlight the critical influence of pore architecture on mechanical performance, with the Voronoi and strut designs demonstrating more favorable stress profiles for bone scaffold applications compared to the conventional curved design.

4. Discussion

Treating large bone defects has long been a challenge for clinicians, and investigating bone tissue engineering and cancellous bone regeneration remains a hot research topic. Porous scaffolds have recently been recognized as some of the best tools for structural and functional healing of bone defects because of their immediate and lasting stability, along with excellent osteogenic properties.[25,26] Ensuring the immediate stability of bone implants, especially preventing peri-implant bone collapse that can weaken prosthetic stability, is a critical challenge in modern orthopedics. As a result, much effort is directed toward improving osseointegration through structural improvements, surface modifications, and complementary approaches.[27–29]

Our previous work demonstrated the feasibility of fabricating precise titanium scaffolds using SLM and investigated the early osseointegration potential and mechanical properties of conventional porous scaffold structures.[19] Concurrently, extensive research investigates geometry-based architectures in bone scaffolds designed via image-based structure modeling or CAD, predominantly emphasizing mechanical behavior and *in vitro* performance.[11,30,31] Nevertheless, native osseous

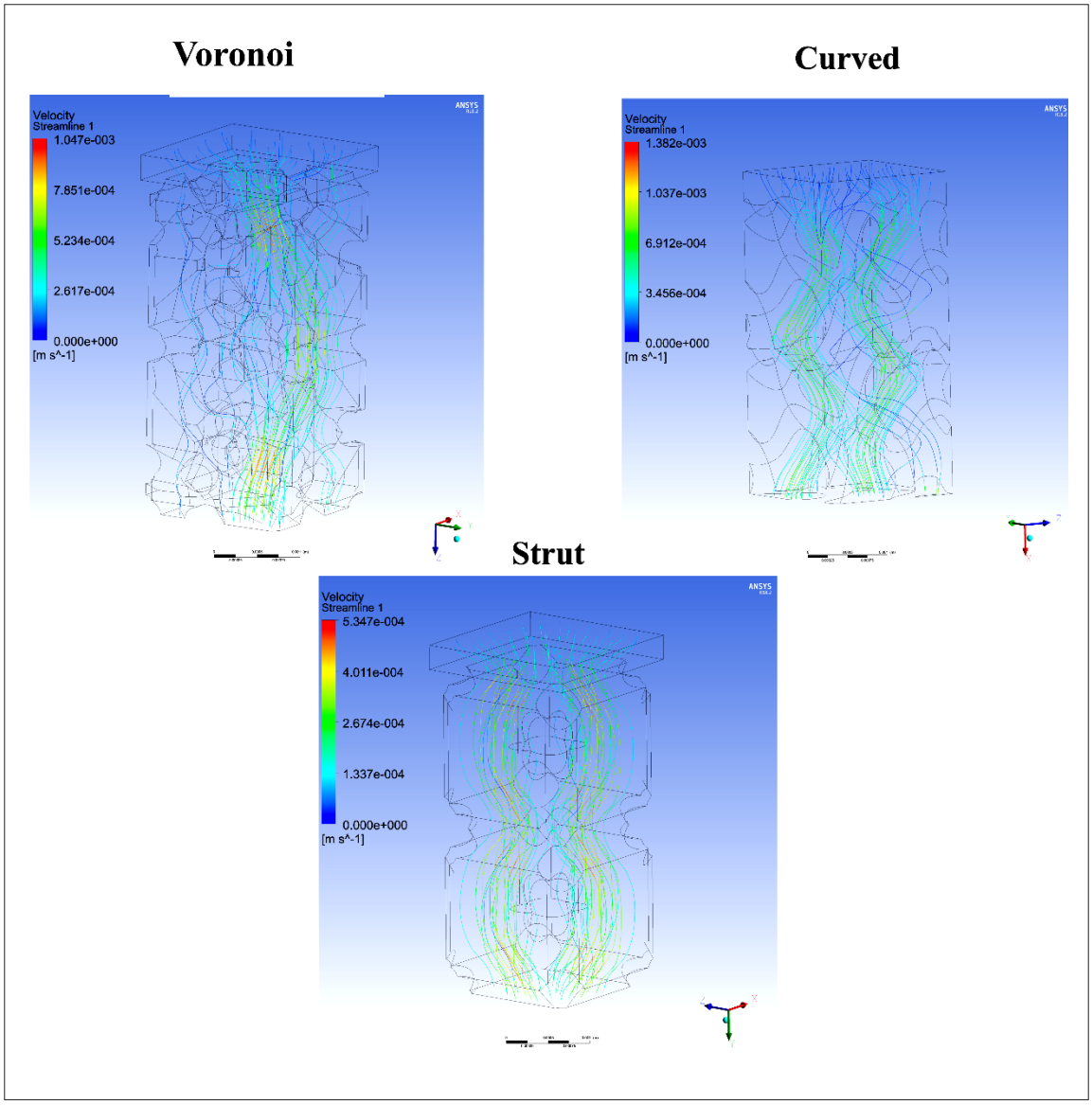

Figure 8. Velocity flow diagrams for the three scaffolds tested.

tissue exhibits intrinsically irregular Voronoi architecture and heterogeneous pore distribution—morphological features conferring biomechanically and osteogenically optimized functionality.[32,33] While CT-derived biomimetic constructs provide anatomical relevance, their clinical translation remains constrained by site-specific anatomical variations in bone microstructure and mechanical requirements. The Voronoi algorithm enables parametric design of biomimetic cancellous bone scaffolds, offering computational tractability and morphological fidelity.[34–36] Since its inception, this approach has been broadly adopted in orthopedic engineering. Voronoi scaffold architecture demonstrates superior mechanical strength and enhanced load transfer efficiency compared to conventional strut-based and gyroid TPMS designs.[37,38] This performance advantage aligns with the physiological load-bearing mechanisms inherent to human skeletal systems.[39]

To assess early osteogenic potential, a systematic comparison was made among three Ti6Al4V scaffold architectures with 60% porosity: Voronoi-based, conventional strut-based, and curved designs. Following implantation of the scaffolds in rabbit femoral condyles, osseointegration dynamics were quantitatively analyzed

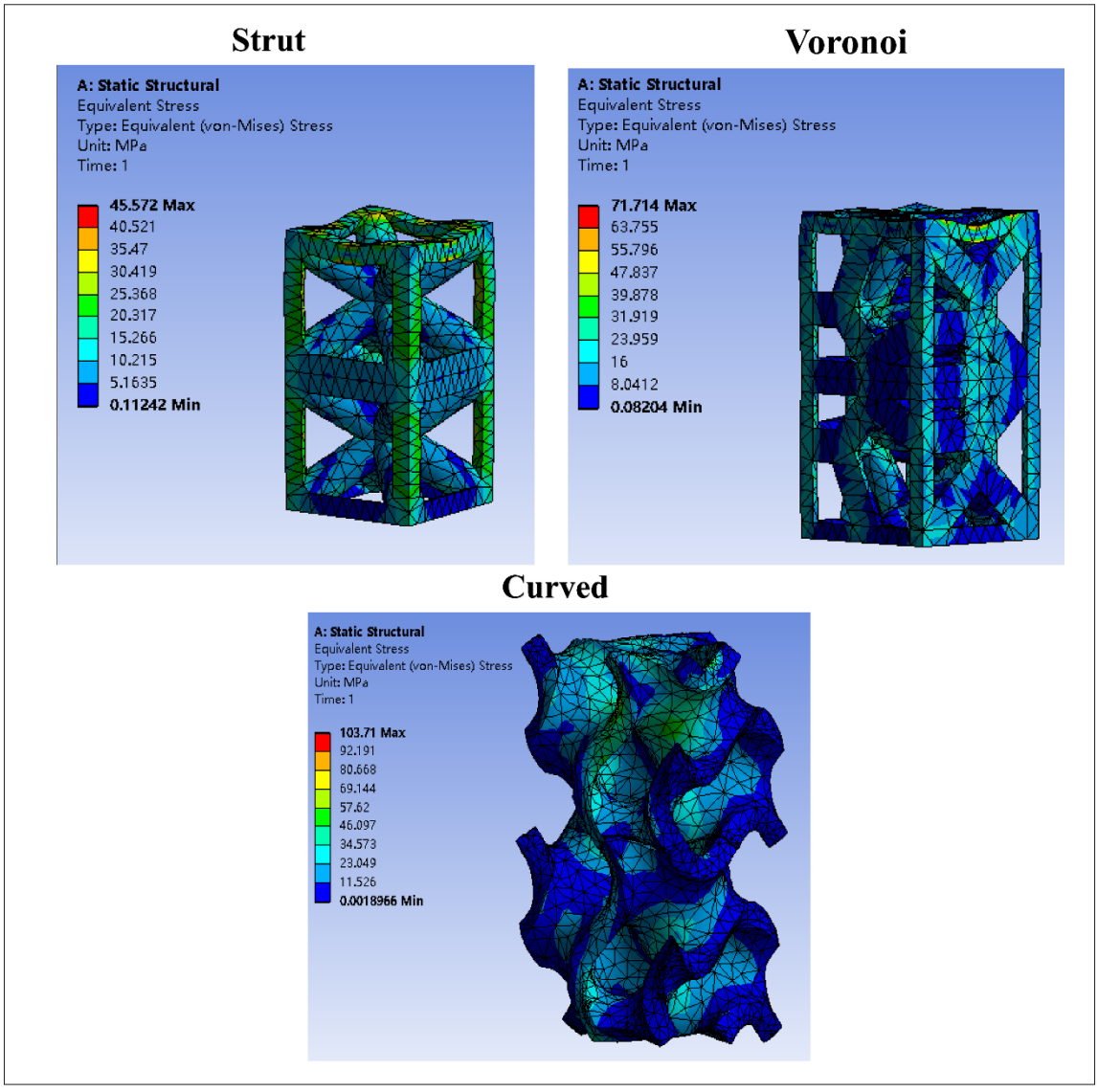

Figure 9. Finite element analysis of the compression test results.

to identify optimal bone-regenerative architectures. CFD simulations were utilized to characterize scaffold permeability, velocity profiles, and flow trajectories. The synergistic integration of *in vivo* experimentation and CFD analysis elucidated structure-dependent osteogenic mechanisms, thereby establishing a novel framework for biomimetic scaffold design.

Considering the influence of materials on osseointegration, Ti6Al4V material, which is biocompatible and promising for a wide range of applications, was used to prepare bone scaffolds in this study, and all the scaffolds were successfully prepared by SLM 3D printing and showed different structural characteristics. Prior to *in vivo* implantation, biomechanical characterization was used to quantify the elastic modulus and yield strength of all scaffold architectures. Scaffold moduli (0.1–4.5 GPa) were found to align with established cancellous bone properties, allowing for mitigation of stress shielding risks through modulus matching. All constructs demonstrated yield strengths exceeding 100 MPa, which significantly surpass documented values for vertebral and femoral cancellous bone, satisfying the mechanical demands of orthopedic implantation.

Quantitative analysis of the histological results confirmed progressive osseous tissue deposition within all scaffold groups during the intervals at weeks 4 and 12. Voronoi constructs demonstrated significantly enhanced osseointegration compared to curved and strut-based designs at both endpoints. These findings were corroborated with micro-CT volumetry data, with BV/TV ratios revealing superior bony ingrowth in Voronoi architectures ($p < 0.01$). Given the precise control over the porosity of the porous scaffolds, the most likely cause of this osteogenic difference is the pore shape. Van Bael et al.[10] found that circular pore structures are more prone to pore plugging than non-circular pore structures based on *in vitro* results. The disparity in pore architecture may influence the transport of nutrients and oxygen within the scaffold, thereby affecting the efficacy of bone regeneration. The suboptimal osteogenic performance of strut-based structures could be attributed to their pore characteristics. In contrast, the Voronoi algorithm-based bionic trabecular configuration demonstrates enhanced osteogenic potential, likely due to its structural resemblance to the native human trabecular bone. We posit this osteogenic superiority originates from biomimetic stochastic morphology: Voronoi-generated trabecular analogs recapitulate cancellous bone's structural heterogeneity, and might facilitate angiogenic–osteogenic coupling while providing osteoconductive topographical cues for cellular adhesion and proliferation.

To elucidate the structural influences on osteogenesis, we utilized CFD simulations to characterize the kinetics of scaffold perfusion and interstitial flow profiles.[40] Following osseous injury, vascular infiltration delivering osteoprogenitor cells and nutrients must permeate the implant architecture to initiate regeneration, where initial osteoblast adhesion dictates the subsequent potential for osseointegration.[41] Consequently, beyond biomechanical competence, fluid mechanics properties constitute a critical determinant of scaffold conductivity. CFD pressure distribution analysis reveals distinct hemodynamic environments across scaffold architectures. The strut configuration exhibits the most moderate pressure gradient (ΔP), while the G-surface-based design demonstrates significantly elevated ΔP. This disparity suggests significant flow impedance in strut architectures, potentially compromising perfusion efficiency.[42] Crucially, this pressure differential directly correlates with fluid shear stress magnitude, a potent mechanical regulator of osteogenic differentiation.[43,44] Consequently, Curved and Voronoi topologies promote substantially enhanced osteogenic efficiency compared to strut structures. Velocity flow diagrams demonstrated reduced intraluminal flow rates in Voronoi designs—a hemodynamic environment conducive to cellular adhesion. Permeability quantification via Darcy's law showed the following hierarchy: strut > Voronoi > curved. We posit that elevated permeability in strut scaffolds enhances mass transport but impedes cellular retention. Conversely, curved architecture promotes cell adhesion at the expense of restricted nutrient exchange.[45] The Voronoi structure approximates the structure of human cancellous bone, achieving an optimal balance between perfusion efficiency and cell retention by balancing the permeability and pressure gradient, which serves as the plausible reason for its superior osteogenic efficacy.[37]

The finite element analysis results provided critical insights into the mechanical behavior of the scaffolds under compressive load, corroborating and explaining the *in vivo* performance. The significantly lower maximum von Mises stress observed in the Voronoi scaffold (45.57 MPa) compared to the strut (103.71 MPa) and curved structures (71.71 MPa) indicates its superior ability to distribute stress more evenly throughout its architecture. This reduced stress concentration is a direct consequence of its biomimetic, stochastic trabecular-like design, which effectively mitigates localized stress peaks that could lead to micro-damage or implant failure over time. More importantly, this mechanical environment is conducive to bone remodeling, as it more closely mimics the physiological stress distribution in natural cancellous bone, thereby reducing the risk of stress-shielding-induced bone resorption. This advantageous stress profile, combined with its optimal permeability and fluid dynamics as revealed by CFD, creates a synergistic mechanobiological microenvironment that promotes enhanced cellular activity and osteogenesis, ultimately explaining the superior BV/TV ratio and osseointegration observed in the Voronoi group.

The current study strongly supports that Voronoi algorithm-based biomimetic bone trabecular scaffolds enhance early osseointegration. Micro-CT (BV/TV) and histological analyses demonstrated superior osteogenic potential, with the Voronoi scaffold inducing significantly greater new bone formation at 4 and 12 weeks post-implantation compared with the curved or traditional pillar structures. This advantage stems from the biomimetic replication of natural trabeculae's random, non-periodic topology, which fosters a microenvironment conducive to cell adhesion, migration, differentiation, and enhanced vascularization/nutrient delivery via optimized fluid dynamics. CFD simulations revealed significantly lower internal ΔP alongside more uniform, reduced flow velocities within the Voronoi scaffold, closely approximating physiological conditions suitable for promoting cell adhesion/retention. Conversely, the pillar

structure exhibited high ΔP and localized high-velocity flows impairing perfusion and cell retention, while the curved structure's low permeability potentially restricted deep nutrient supply. The Voronoi scaffold's intermediate permeability κ suggests an optimal balance for nutrient exchange and cell retention.

While this study demonstrates the promising biomechanical performance and early osseointegration capabilities of Ti6Al4V scaffolds based on the Voronoi designed, several limitations warrant consideration. Firstly, the use of healthy rabbit femoral condyles as experimental models may limit direct extrapolation to complex clinical scenarios involving comorbidities such as osteoporosis or diabetes, where bone regeneration dynamics differ significantly. Secondly, the evaluation period, restricted to 12 weeks post-implantation, provides valuable insights into early-stage tissue response but precludes a comprehensive assessment of long-term structural stability and functional integration. Future studies could explore the integration of topology optimization algorithms with Voronoi tessellation to further refine pore morphology and mechanical stimuli distribution for enhancing biological performance.[46] Long-term animal experiments are also required to investigate specific structural osteogenic mechanisms, aiming to optimize scaffold design for varied clinical applications. Addressing these gaps is essential to translate promising preclinical results into clinically viable solutions for complex bone regeneration challenges.

5. Conclusion

The Voronoi design offers a potent biomimetic strategy for fabricating porous titanium alloy-based bone scaffolds with enhanced osteogenesis properties, which demonstrates superior potential compared to the strut and curved structures in promoting bone defect repair, particularly in situations where rapid osseointegration is crucial. Through future integration of surface functionalization, multi-scale gradients, and patient-specific optimization, bionic scaffolds based on Voronoi design would provide a promising platform for next-generation bone tissue engineering in future.

Acknowledgments

None.

Funding

This study was supported by the Sichuan Science and Technology Program (2024YFHZ0067; awarded to J.L.) and the China Postdoctoral Science Foundation (2023MD744134; awarded to L.L.).

Conflict of interest

All authors report no conflicts of interest relevant to the contents of this paper.

Author contributions

Conceptualization: Jinghong Yang, Zi Wang
Formal analysis: All authors
Investigation: All authors
Methodology: All auhors
Writing–original draft: Jinghong Yang
Writing–review & editing: Linlin Liu, Juncai Liu, Zhong Li
All authors have read and agreed to the published version of the manuscript.

Ethics approval and consent to participate

This study was approved by the Ethics Committee of the Affiliated Hospital of Southwest Medical University and conducted in adherence to the principles set forth in the Declaration of Helsinki.

Consent for publication

Not applicable.

Availability of data and materials

The datasets used and/or analyzed during the current study are available from the corresponding author upon reasonable request.

References

1. Jing Z, Zhang T, Xiu P, et al. Functionalization of 3D-printed titanium alloy orthopedic implants: a literature review. *Biomed Mater*. 2020;15(5):052003. doi: 10.1088/1748-605X/ab9078
2. Li L, Shi J, Zhang K, et al. Early osteointegration evaluation of porous Ti6Al4V scaffolds designed based on triply periodic minimal surface models. *J Orthop Translat*. 2019;19:94-105. doi: 10.1016/j.jot.2019.03.003
3. Revilla-León M, Meyer MJ, Özcan M. Metal additive manufacturing technologies: literature review of current status and prosthodontic applications. *Int J Comput Dent*. 2019;22(1):55-67.
4. Alammar A, Kois JC, Revilla-León M, Att W. Additive Manufacturing Technologies: Current Status and Future Perspectives. *J Prosthodont*. 2022;31(S1):4-12. doi: 10.1111/jopr.13477
5. Liu F, Ran Q, Zhao M, Zhang T, Zhang DZ, Su Z. Additively manufactured continuous cell-size gradient porous scaffolds: pore characteristics, mechanical properties and biological responses in vitro. *Materials (Basel)*. 2020;13(11):2589.

doi: 10.3390/ma13112589

6. Ran Q, Yang W, Hu Y, et al. Osteogenesis of 3D printed porous Ti6Al4V implants with different pore sizes. *J Mech Behav Biomed Mater*. 2018;84:1-11. doi: 10.1016/j.jmbbm.2018.04.010
7. Arjunan A, Demetriou M, Baroutaji A, Wang C. Mechanical performance of highly permeable laser melted Ti6Al4V bone scaffolds. *J Mech Behav Biomed Mater*. 2020;102:103517. doi: 10.1016/j.jmbbm.2019.103517
8. Wang H, Su K, Su L, Liang P, Ji P, Wang C. The effect of 3D-printed Ti(6)Al(4)V scaffolds with various macropore structures on osteointegration and osteogenesis: a biomechanical evaluation. *J Mech Behav Biomed Mater*. 2018;88:488-496. doi: 10.1016/j.jmbbm.2018.08.049
9. Gryko A, Prochor P, Sajewicz E. Finite element analysis of the influence of porosity and pore geometry on mechanical properties of orthopaedic scaffolds. *J Mech Behav Biomed Mater*. 2022;132:105275. doi: 10.1016/j.jmbbm.2022.105275
10. Van Bael S, Chai YC, Truscello S, et al. The effect of pore geometry on the in vitro biological behavior of human periosteum-derived cells seeded on selective laser-melted Ti6Al4V bone scaffolds. *Acta Biomater*. 2012;8(7):2824-34. doi: 10.1016/j.actbio.2012.04.001
11. Chen Z, Yan X, Yin S, et al. Influence of the pore size and porosity of selective laser melted Ti6Al4V ELI porous scaffold on cell proliferation, osteogenesis and bone ingrowth. *Mater Sci Eng C Mater Biol Appl*. 2020;106:110289. doi: 10.1016/j.msec.2019.110289
12. Coburn B, Salary RR. Mechanical characterization of porous bone-like scaffolds with complex microstructures for bone regeneration. *Bioengineering (Basel)*. 2025;12(4):416. doi: 10.3390/bioengineering12040416
13. Kumar PV, Pal S, Birru AK, Jaganathan BG, Muthu N. 3D-printed TPMS-structured hybrid PLA/MgTiO(3) scaffolds: Synergizing bioactivity and antibacterial performance for bone regeneration. *Biomater Adv*. 2025;177:214370. doi: 10.1016/j.bioadv.2025.214370
14. Pazhamannil RV, Alkhedher M. Advances in additive manufacturing for bone tissue engineering: materials, design strategies, and applications. *Biomed Mater*. 2024;20(1). doi: 10.1088/1748-605X/ad9dce
15. Ma J, Li Y, Mi Y, et al. Novel 3D printed TPMS scaffolds: microstructure, characteristics, and applications in bone regeneration. *J Tissue Eng*. 2024;15:20417314241263689. doi: 10.1177/20417314241263689
16. Ye J, Miao B, Xiong Y, et al. 3D printed porous magnesium metal scaffolds with bioactive coating for bone defect repair: enhancing angiogenesis and osteogenesis. *J Nanobiotechnology*. 2025;23(1):160. doi: 10.1186/s12951-025-03222-3
17. Hao W, Yongtao L, Jian J, Hanxing Z. Data-driven inverse design of novel spinodoid bone scaffolds with highly matched mechanical properties in three orthogonal directions. *Mater Des*. 2025;251:113697. doi: 10.1016/j.matdes.2025.113697
18. Amini AR, Laurencin CT, Nukavarapu SP. Bone tissue engineering: recent advances and challenges. *Crit Rev Biomed Eng*. 2012;40(5):363-408. doi: 10.1615/critrevbiomedeng.v40.i5.10
19. Deng F, Liu L, Li Z, Liu J. 3D printed Ti6Al4V bone scaffolds with different pore structure effects on bone ingrowth. *J Biol Eng*. 2021;15(1):4. doi: 10.1186/s13036-021-00255-8
20. Vossenberg P, Higuera GA, van Straten G, van Blitterswijk CA, van Boxtel AJ. Darcian permeability constant as indicator for shear stresses in regular scaffold systems for tissue engineering. *Biomech Model Mechanobiol*. 2009;8(6):499-507. doi: 10.1007/s10237-009-0153-6
21. Sinha R, Le Gac S, Verdonschot N, van den Berg A, Koopman B, Rouwkema J. Endothelial cell alignment as a result of anisotropic strain and flow induced shear stress combinations. *Sci Rep*. 2016;6:29510. doi: 10.1038/srep29510
22. Ali D. Effect of scaffold architecture on cell seeding efficiency: a discrete phase model CFD analysis. *Comput Biol Med*. 2019;109:62-69. doi: 10.1016/j.compbiomed.2019.04.025
23. Melchels FP, Tonnarelli B, Olivares AL, et al. The influence of the scaffold design on the distribution of adhering cells after perfusion cell seeding. *Biomaterials*. 2011;32(11): 2878-2884. doi: 10.1016/j.biomaterials.2011.01.023
24. Beaudoin AJ, Mihalko WM, Krause WR. Finite element modelling of polymethylmethacrylate flow through cancellous bone. *J Biomech*. 1991;24(2):127-136. doi: 10.1016/0021-9290(91)90357-s
25. Sun J, Chen C, Zhang B, Yao C, Zhang Y. Advances in 3D-printed scaffold technologies for bone defect repair: materials, biomechanics, and clinical prospects. *Biomed Eng Online*. 2025;24(1):51. doi: 10.1186/s12938-025-01381-w
26. Zhang L, Yang G, Johnson BN, Jia X. Three-dimensional (3D) printed scaffold and material selection for bone repair. *Acta Biomater*. 2019;84:16-33. doi: 10.1016/j.actbio.2018.11.039
27. Attarilar S, Ebrahimi M, Djavanroodi F, Fu Y, Wang L, Yang J. 3D printing technologies in metallic implants: a thematic review on the techniques and procedures. *Int J Bioprint*. 2021;7(1):306. doi: 10.18063/ijb.v7i1.306

28. Distefano F, Pasta S, Epasto G. Titanium lattice structures produced via additive manufacturing for a bone scaffold: a review. *J Funct Biomater*. 2023;14(3):125. doi: 10.3390/jfb14030125

29. Elhattab K, Hefzy MS, Hanf Z, et al. Biomechanics of additively manufactured metallic scaffolds-a review. *Materials (Basel)*. 2021;14(22):6833. doi: 10.3390/ma14226833

30. Wang C, Xu D, Lin L, et al. Large-pore-size Ti6Al4V scaffolds with different pore structures for vascularized bone regeneration. *Mater Sci Eng C Mater Biol Appl*. 2021;131:112499. doi: 10.1016/j.msec.2021.112499

31. Zhao F, Xiong Y, Ito K, van Rietbergen B, Hofmann S. Porous geometry guided micro-mechanical environment within scaffolds for cell mechanobiology study in bone tissue engineering. *Front Bioeng Biotechnol*. 2021;9:736489. doi: 10.3389/fbioe.2021.736489

32. Fonseca H, Moreira-Gonçalves D, Coriolano HJ, Duarte JA. Bone quality: the determinants of bone strength and fragility. *Sports Med*. 2014;44(1):37-53. doi: 10.1007/s40279-013-0100-7

33. Müller R. Hierarchical microimaging of bone structure and function. *Nat Rev Rheumatol*. 2009;5(7):373-381. doi: 10.1038/nrrheum.2009.107

34. Gómez S, Vlad MD, López J, Fernández E. Design and properties of 3D scaffolds for bone tissue engineering. *Acta Biomater*. 2016;42:341-350. doi: 10.1016/j.actbio.2016.06.032

35. Zhao Z, Li J, Yao D, Wei Y. Mechanical and permeability properties of porous scaffolds developed by a Voronoi tessellation for bone tissue engineering. *J Mater Chem B*. 2022;10(46):9699-9712. doi: 10.1039/d2tb01478e

36. Zou S, Gong H, Gao J. Additively manufactured multilevel voronoi-lattice scaffolds with bonelike mechanical properties. *ACS Biomater Sci Eng*. 2022;8(7):3022-3037. doi: 10.1021/acsbiomaterials.1c01482

37. Mamuti M, Chao L, Tian Z. Analysis of mechanical characteristics and permeability of TPMS and Voronoi porous structure for bone scaffold. *Comput Methods Biomech Biomed Engin*. 2024:1-14. doi: 10.1080/10255842.2024.2358378

38. Zhu L, Liang H, Lv F, et al. Design and compressive fatigue properties of irregular porous scaffolds for orthopedics fabricated using selective laser melting. *ACS Biomater Sci Eng*. 2021;7(4):1663-1672. doi: 10.1021/acsbiomaterials.0c01392

39. Morgan EF, Unnikrisnan GU, Hussein AI. Bone mechanical properties in healthy and diseased states. *Annu Rev Biomed Eng*. 2018;20:119-143. doi: 10.1146/annurev-bioeng-062117-121139

40. Channasanon S, Kaewkong P, Chantaweroad S, et al. Scaffold geometry and computational fluid dynamics simulation supporting osteogenic differentiation in dynamic culture. *Comput Methods Biomech Biomed Engin*. 2024;27(5):587-598. doi: 10.1080/10255842.2023.2195961

41. Prakoso AT, Basri H, Adanta D, et al. The effect of tortuosity on permeability of porous scaffold. *Biomedicines*. 2023;11(2):427. doi: 10.3390/biomedicines11020427

42. Lai R, Jiang J, Huo Y, et al. Design of novel graded bone scaffolds based on triply periodic minimal surfaces with multi-functional pores. *Front Bioeng Biotechnol*. 2025;13:1503582. doi: 10.3389/fbioe.2025.1503582

43. Pei T, Su G, Yang J, et al. Fluid shear stress regulates osteogenic differentiation via annexina6-mediated autophagy in MC3T3-E1 cells. *Int J Mol Sci*. 2022;23(24):15702. doi: 10.3390/ijms232415702

44. Zhao Y, Richardson K, Yang R, et al. Notch signaling and fluid shear stress in regulating osteogenic differentiation. *Front Bioeng Biotechnol*. 2022;10:1007430. doi: 10.3389/fbioe.2022.1007430

45. Ferguson BM, Clark JR, Li Q. Scaffold geometries designed to promote bone ingrowth by enhancing mechanobiological stimulation and biotransportation - a multiobjective optimisation approach. *J Mech Behav Biomed Mater*. 2025;164:106883. doi: 10.1016/j.jmbbm.2024.106883

46. Liu B, Feng J, Chen J, He Y, Fu J. A topology optimisation-based design method for 3D Voronoi porous structures and its application for medical pillows. *Virtual Phys Prototyp*. 2023;18(1):e2285392. doi: 10.1080/17452759.2023.2285392